



Effect of composition ratio on the structural and optical properties of MnS@ZnS nanocomposites

Zein K. Heiba¹ · Mohamed Bakr Mohamed^{1,2} · S. I. Ahmed^{1,3} · A. M. El-naggar^{1,4} · AA. Albassam⁴

Received: 4 May 2020 / Accepted: 17 July 2020 / Published online: 25 July 2020
© Springer Science+Business Media, LLC, part of Springer Nature 2020

Abstract

Nanocomposites $(1-x)\text{MnS}-x\text{ZnS}$ ($x=0, 0.25, 0.5, 0.75, 1$) heterostructures were synthesized by a simple chemical procedure at low temperature (300 °C). The influence of the alloying ratio (x) on the phases developed was investigated utilizing the Rietveld X-ray diffraction (XRD) analysis and Fourier transform infrared (FTIR). Zinc sulfide crystallized in one phase having zincblende structure, while manganese sulfide was formed in three phases having cubic and hexagonal structures. The determined crystallite size for ZnS was in the range 3–4 nm, resembling quantum dots, while for the cubic MnS phase the size was bigger in the range 15–20 nm, and it is much bigger for MnS hexagonal phase, about 76 nm. A High-resolution transmission electron microscope (HRTEM) images confirmed the big difference in particle sizes of MnS and ZnS. The UV diffused reflectance was obviously affected by the ratio of MnS to ZnS in the matrix; the intermediate composites (0.25, 0.5, and 0.75) had bandgap energy less than those of pure MnS and ZnS. The refractive index value was influenced by the degree of crystallinity and density of the samples. Photoluminescence (PL) analysis revealed high dependence on the sample composition with ZnS and the intermediate composites samples had broader spectra compared to the MnS sample; the intermediate samples were blue shifted. Also, PL intensities of intermediate nanocomposites were less than those of MnS and ZnS samples.

1 Introduction

Semiconductor nanomaterials doped with Mn ions have been widely studied due to their optical characteristics which nominate it to be used in several optoelectronic and bio-imaging applications [1]. MnS is a wide bandgap (3.2 eV) semiconductor material which has exchange-coupling between Mn–Mn pairs [2]. Manganese sulfide usually

exists as MnS_2 (cubic), β -MnS (zinc blende), γ -MnS (wurtzite), and α -MnS (rock salt) polymorphs [3, 4]. Meanwhile, zinc sulfide (ZnS) has also a large direct bandgap around 3.8 eV, a small exciton Bohr radius of 2.5 nm with a large exciton binding energy (40 meV), and a high refractive index ($n=2.57$) [5, 6]. Therefore, it can be used in different applications such as ultraviolet light-emitting diodes, electro-luminescence devices, panel displays, sensors, and injection lasers [7]. ZnS can crystallize into two types of structural forms: hexagonal and cubic phases [5]. Doping II-VI semiconductors with Mn ions has been widely studied [8]. Furthermore, there are new opportunities for modulating the bandgaps of Mn-based ternary chalcogenide nanowires and promoting their further application in photonics and spintronics [5]. Doping ZnS with Mn^{2+} has been attracted great attention [8]. Mn^{2+} doping can not only enhance its optical transition efficiency but also persuade remarkable magneto-optical characteristics of the host matrix [8]. For example, Cai et al. found that the ternary alloyed $\text{Zn}_{1-x}\text{Mn}_x\text{S}$ nanowires have bandgaps followed the non-linear bowing character versus the composition [9]. Unfortunately, due to the high surface-to-volume ratio in a nanomaterial, the surface states may operate as luminescence quenching centers,

✉ Zein K. Heiba
zein_kh@yahoo.com

✉ Mohamed Bakr Mohamed
mbm1977@yahoo.com

¹ Physics Department, Faculty of Science, Ain Shams University, Cairo, Egypt

² Physics Department, Faculty of Science, Taibah University, Al-Madina al Munawarah, Saudi Arabia

³ Physics Department, Faculty of Science, Taif University, Taif 21974, Saudi Arabia

⁴ Research Chair of Exploitation of Renewable Energy Applications in Saudi Arabia, Physics and Astronomy Department, College of Science, King Saud University, P.O. Box 2455, Riyadh 11451, Saudi Arabia

resulting in low luminescence efficiency [9]. Peng's group developed a new doping approach such as the nucleation doping process [10, 11]. For example, Mn-doped ZnSe was prepared by formed ZnSe shell on MnSe core, the photoluminescence quantum yield (PL QY) of the obtained material was enhanced up to 50% with good thermal stability [10, 11]. This method significantly improves the PL QY of the doped nanomaterials by controlling the diffusion of Mn ions in the nanomaterials and the structure of nanomaterials [11]. It was found that the PL QY is greatly influenced by the structural properties of the Mn ion diffusion layer, which is directly determined by the diffusion of Mn ions into the ZnS shell during the colloidal growth process [12]. The core-shell nanostructure of ultrathin MnS shells on nano-ZnS:Mn has an effect in vivo MRI T_1 contrast agents for the gallbladder and pancreas in mice [13]. Yuvaloshini et al. [14] revealed that the annealed ZnS/MnS superlattice thin films have higher absorption, extinction coefficient, optical conductivity and electrical conductivity as compared with non-annealed films. Furthermore, the refractive index has low values regardless of the films were annealed or not, which nominated it to be used in antireflective coating [14]. In the present work, $(1-x)\text{MnS}-x\text{ZnS}$ nanocomposites, $x=0, 0.25, 0.5, 0.75$ and 1 have been prepared by thermolysis procedure. The structural, microstructural and optical behaviors of the studied samples have been investigated in detail using X-ray diffraction (XRD), high-resolution transmission electron microscope (HRTEM), Fourier transform infrared (FTIR) spectrometer, diffuse reflectance and photoluminescence (PL) techniques.

2 Experimental details

Nanocomposites $(1-x)\text{MnS}-x\text{ZnS}$ ($x=0.0, 0.25, 0.5, 0.75, 1$) heterostructures were synthesized by mixing and heating a stoichiometric amount of manganese acetate, zinc acetate and thiourea at 300 °C (2 h) in an electric oven [15–24]. Rietveld profile method [25] was applied to determine the

crystal structure and microstructure of the samples using MAUD software [26] and X-ray diffraction data (XRD) collected by X'pert MPD, Panalytical diffractometer with $\text{Cu-K}\alpha$ (LaB_6 standard was used to correct instrumental broadening). Fourier transform infrared (FTIR), diffuse reflectance, and photoluminescence (PL) spectra of the samples were measured using a Bruker Tensor 27 FTIR spectrometer ($400\text{--}4000\text{ cm}^{-1}$), a double-beam spectrophotometer Shimadzu UV-VIS-2600 (with attached integrating sphere assembly, 190–1400 nm), and a spectrometer RF-1501; Shimadzu, Ltd., respectively. A high-resolution transmission electron microscope (HRTEM) was conducted to investigate the nature of the nanosamples.

3 Results and discussion

3.1 XRD structural analysis

The good quality XRD patterns measured for the present system $(1-x)\text{MnS}-x\text{ZnS}$ heterostructures enabled us from the accurate determination of the phases present in the samples and finding their percentages applying the search match program X'pert HighScore plus. Rietveld analysis was performed and the obtained structural and microstructural parameters are listed in Table 1. Excellent XRD pattern fitting, Fig. 1, was obtained from Rietveld analysis. The pure zinc sulfide exhibited only one phase ZnS $F\bar{4}3m$, and its cell parameter increased with the alloying parameter (x) indicating a tensile strain. The present pure manganese sulfide sample manifested three phases: two cubic: $\alpha\text{-MnS}$ $Fm\bar{3}m$ and MnS_2 $Pa\bar{3}$, and one hexagonal $\gamma\text{-MnS}$ $P6/3m$ c. As shown in Table 1, the nanocomposite samples $(1-x)\text{MnS}-x\text{ZnS}$ ($x=0.25, 0.5$ and 0.75) manifested a combination of the above phases with different percentages. Inspecting Table 1, one can find that the determined crystallite size for ZnS is in the range 3–4 nm, resembling quantum dots, while for the cubic MnS phase the size is bigger in the range 15–20 nm, and it is much bigger for

Table 1 Space group (Sp G), lattice parameters (a, c Å), crystallite size (nm) and sulfur coordinate (z) for $(1-x)\text{MnS}-x\text{ZnS}$ system

x	Manganese sulfide							Zinc Sulfide	
	Cubic			Hexa P 6/3 m c				Cubic $F\bar{4}3m$	
	Sp G	a	Size	a	c	Size	$z(S)$	a	Size
0	$Pa\bar{3}$	6.179 (3)	20	3.983 (2)	6.456 (3)	75	0.3758	–	–
	$Fm\bar{3}m$	5.229	20						
0.25	$F\bar{4}3m$	5.591	16	3.928	6.662	76	0.3998	5.423 (1)	4.0
0.50	$Pa\bar{3}$	6.114	17	–	–	–	–	5.419	3.6
0.75	$Pa\bar{3}$	6.129	15	–	–	–	–	5.376	3.8
1.0	–	–	–	–	–	–	–	5.364	3.6

$Pa\bar{3}$ MnS_2 , $\bar{4}3m$, $Fm\bar{3}m$ and $P6/3m$ c MnS

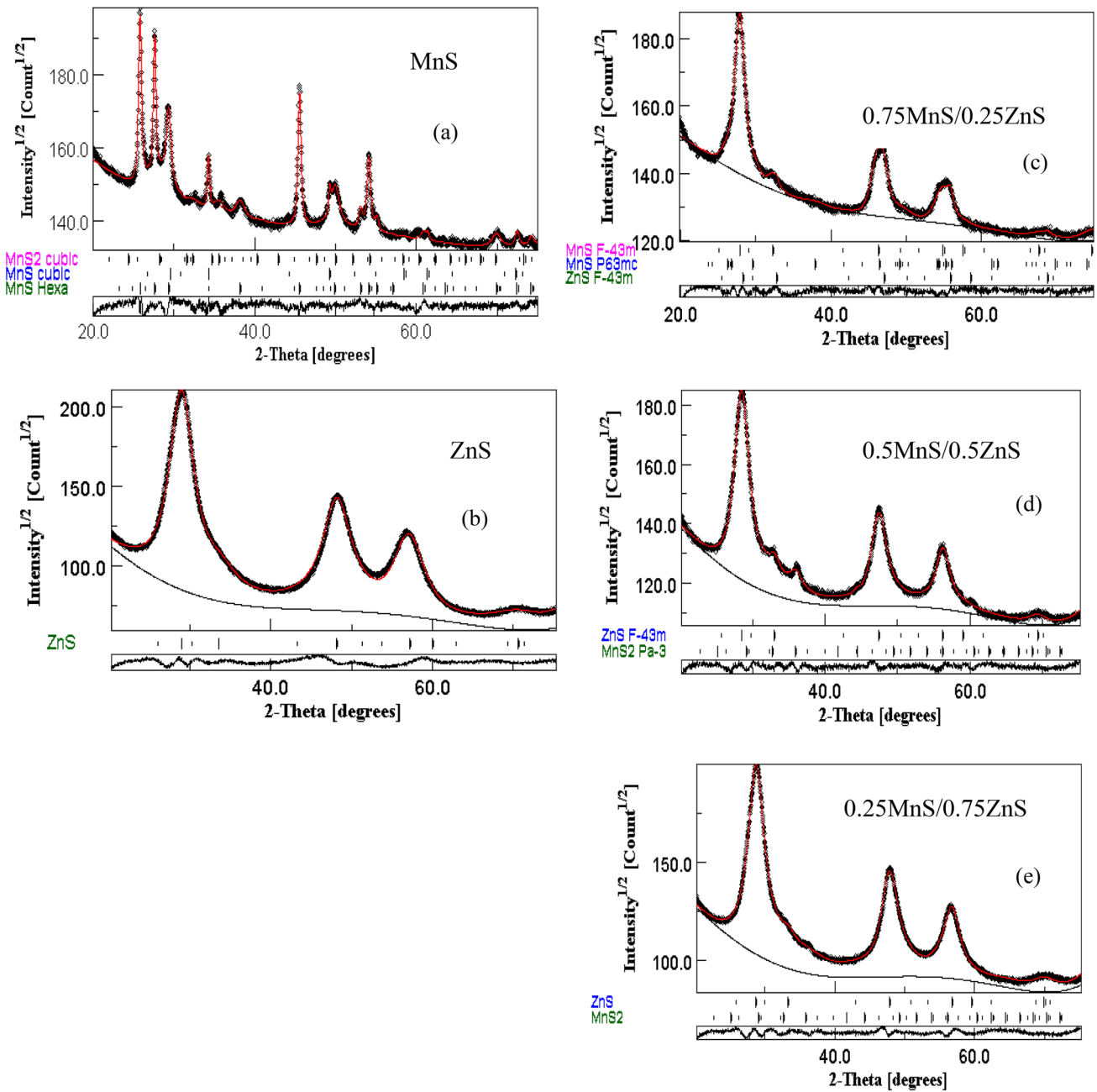


Fig. 1 Rietveld refinements for **a** MnS, **b** ZnS, **c** 0.75MnS/0.25ZnS, **d** 0.5MnS/0.5ZnS, **e** 0.25MnS/0.75ZnS samples

MnS hexagonal phase, about 76 nm. This difference in the size is evident in the HRTEM images, Fig. 2. For pure ZnS, Fig. 2a, the morphology of the particles is homogeneous with a narrow size distribution and high agglomeration. For the nanocomposite with $x=0.5$, Fig. 2b, two distinct regions can be detected for ZnS and MnS which has obvious larger size. Insight of Fig. 2b is the selected area electron diffraction (SAED) pattern where two overlapped patterns can be seen.

3.2 Infrared absorption spectroscopy analysis

Figure 3 represents the FTIR spectra collected at room temperature in the range of $400\text{--}2000\text{ cm}^{-1}$ for MnS, ZnS and $(1-x)\text{MnS}-x\text{ZnS}$ ($x=0.25, 0.5$ and 0.75) heterostructures samples. As revealed from Fig. 3, the intermediate nanocomposite samples have the vibration bands of both MnS and ZnS samples but with different intensities. The absorption bands occurred around 508 and 610 cm^{-1} are

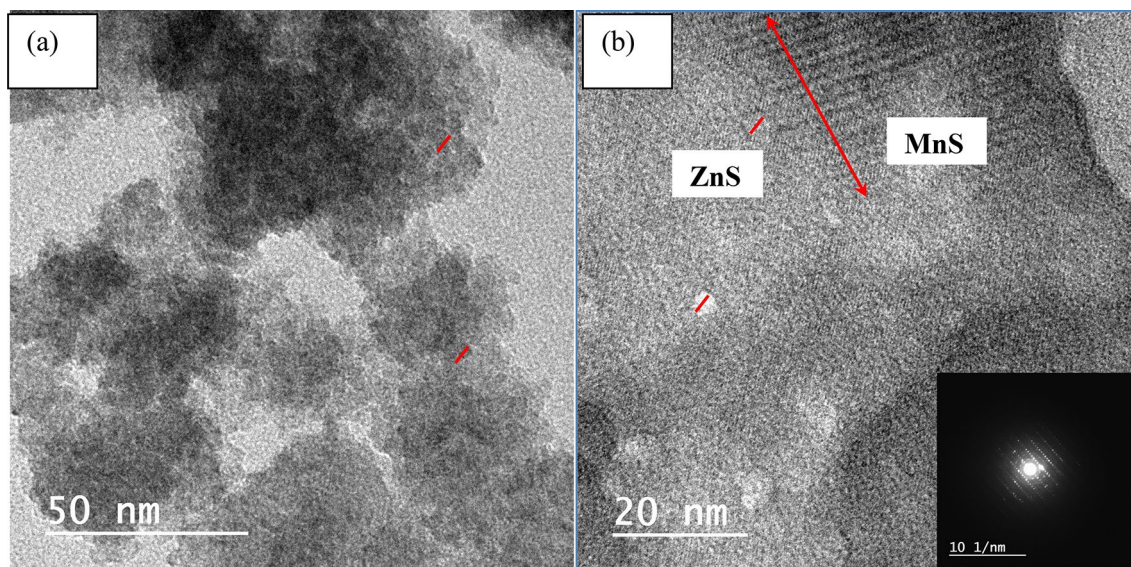


Fig. 2 TEM images for **a** pure ZnS and **b** 0.5MnS/0.5ZnS nanocomposites

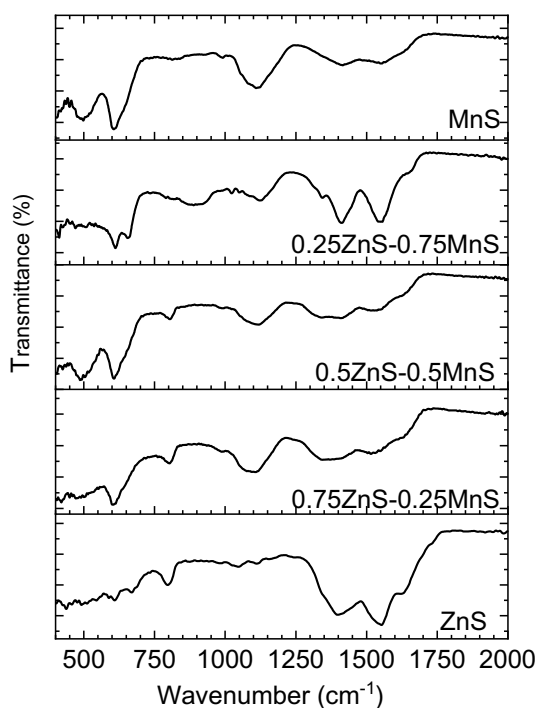


Fig. 3 FTIR spectra of MnS@ZnS heterostructures system

attributed to Mn-S stretch vibrations in γ -MnS and α -MnS phases [27]. The characteristic major bands of pure ZnS are observed in the ranges 432–445 cm^{-1} (asymmetric bending), and 602–613 cm^{-1} (symmetric bending) [28]. Small bands observed from 400 to 500 cm^{-1} are ascribed to the resonance from the interaction between vibrational modes of sulfide ions in the sample [29]. The

C-S linkage stretching vibrations are observed in the region of 700–600 cm^{-1} , while that of S–O–C occurred at 1020 cm^{-1} [30]. The bands observed at 1401–1552 cm^{-1} are characterizing the bands of carboxyl group [31], and at 1631 cm^{-1} from C=O stretching modes; both occurred from the absorption of atmospheric CO_2 on the surface of the nanocrystals [31], respectively. The band observed at about 1099 cm^{-1} in MnS sample is attributed to the C=O of acetates [32].

3.3 UV absorption analysis

Figure 4a reveals the UV diffused reflectance for $(1-x)$ MnS– x ZnS nanocomposites samples with different ratios ($x=0, 0.25, 0.5, 0.75$ and 1) in the wavelength range of 200–800 nm. The 0.5MnS–0.5ZnS sample has the highest reflectance than MnS sample and other composite samples in the wavelength less than 300 nm. Previously, superlattices ZnS/MnS and MnS/ZnS thin films exhibited high reflectance for wavelength less than 300 nm [33] similar to our case. On the other hand, the situation is reversed, where the reflectance is increased for nanocomposites with $x=0.25$ and 0.75 as compared with MnS sample in the wavelength above 500 nm. A possible interpretation for this behavior can argue to the internal structure of the nanocomposite samples itself which plays an essential role in determining the number of defects created inside the materials and hence affects the optical properties of the material.

The bandgap energy (E_g) can be estimated from the relation between absorption coefficient (α) and incident photon energy using the following equations [34]:

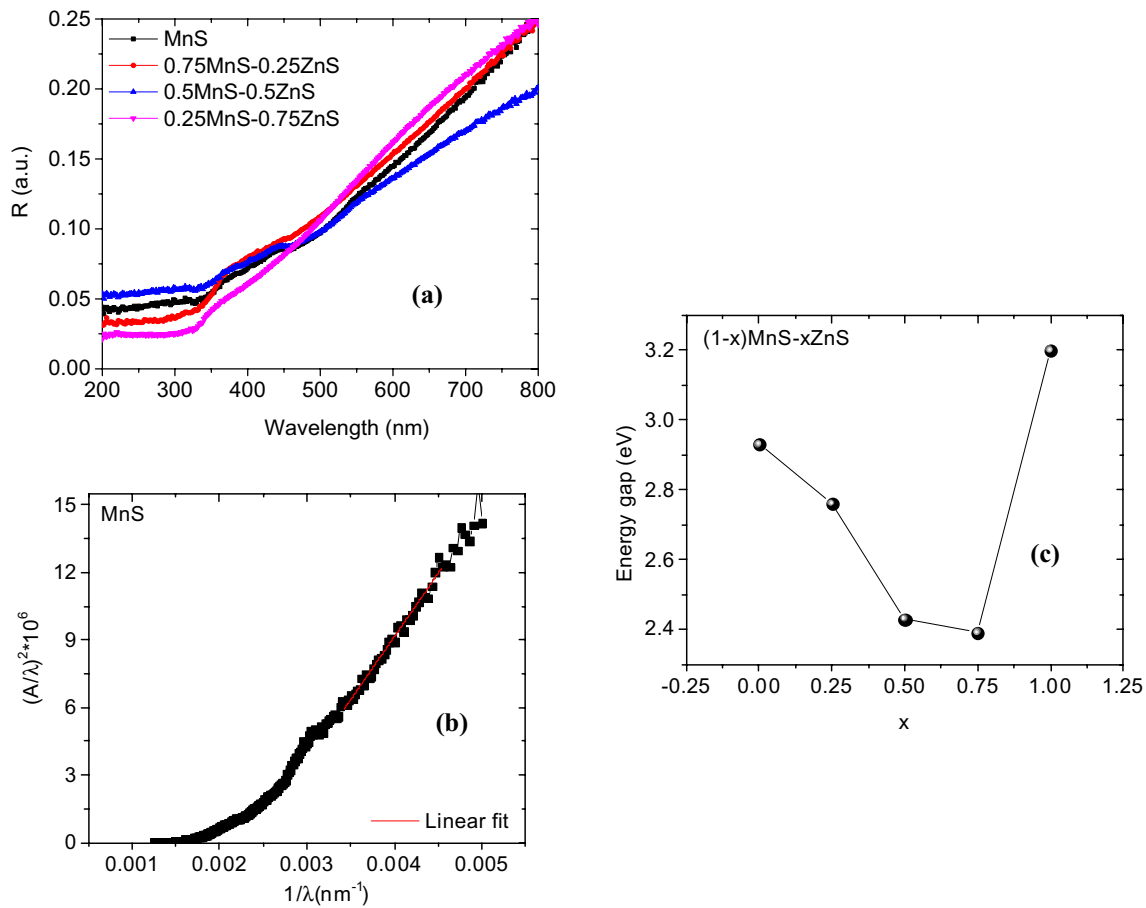


Fig. 4 **a** UV diffused reflectance for MnS@ZnS nanocomposites system, **b** relation between $(A/\lambda)^2$ vs $1/\lambda$ to calculate energy gap for MnS sample and **c** energy gap dependence on composition ratio (x) in MnS@ZnS heterostructures system

$$\alpha h\nu = B(h\nu - E_g)^n \quad (1)$$

$$\alpha = \frac{2.303A}{d} \quad (2)$$

where A , d , E_g , B , $h\nu$ are the absorbance, thickness, optical bandgap, a constant and the incident photon energy, respectively. The refractive index n has a value of 0.5 and 2 for direct and indirect transitions.

Equation (1) can rewrite as the following:

$$\alpha = B(hc)^{n-1} \lambda \left(\frac{1}{\lambda} - \frac{1}{\lambda_g} \right)^n \quad (3)$$

where λ_g , h and c are the wavelength corresponding to the optical energy gap, Plank's constant and light velocity, respectively.

Equation (3) can be rewritten using the Beer–Lambert's law as follows:

$$A(\lambda) = D_1 \lambda \left(\frac{1}{\lambda} - \frac{1}{\lambda_g} \right)^n + D_2 \quad (4)$$

where $D_1 = [B(hc)^{n-1} d/2.303]$ and D_2 is a constant that takes into account the reflection.

Using Eq. (4), the optical bandgap can be obtained without needing the film thickness. The value of λ_g and hence $E_g = 1239.83/\lambda_g$ can be obtained by extrapolating the linear part of $(A/\lambda)^{1/n}$ vs. $(1/\lambda)$ curve at $(A/\lambda)^{1/n} = 0$, Fig. 4b. The obtained bandgap energies for the samples are plot in Fig. 4c. The direct bandgap energy of MnS, 0.75MnS–0.25ZnS, 0.75MnS–0.25ZnS, 0.75MnS–0.25ZnS and ZnS are 2.93, 2.76, 2.43, 2.39 and 3.2 eV, respectively. It was interesting that the obtained bandgaps of $(1-x)$ MnS– x ZnS nanocomposites did not show a linear relationship with the composition x , but exhibited a non-linear optical bowings effect (Fig. 4c) similar to that reported in $Zn_{1-x}Mn_x$ nanowires [9],

PbS_xSe_{1-x} nanocrystals [35] and ZnSe_xTe_{1-x} nanowires [36].

Taking into accounts of the optical bowing effect, the optical absorption and emission of the parent compounds could be tailored and tuned into the visible region through the formation of nanocomposites. Similar results obtained for CuS/CdS(H)/CdS(C) nanocomposites [37]. Ai et al. attributed the decrease in the bandgap of hexagonal/cubic CdS composite is due to the junction formed between the hexagonal and cubic phases of CdS [38]. Michae et al. [39] reported a bandgap shift from UV to the visible region for ZnS–Cu₂S nanoflakes obtained by assisted wet chemical synthesis. The shift of absorption toward visible region was attributed to the impurity level band structures introduced by the presence of Cu₂S in ZnS system. For the present (1-x) MnS–xZnS nanocomposites, the bowing effects, similar to the literatures [9, 35, 36], could arise from the differences in electronegativities, atomic radii, and also the lattice constants between MnS and ZnS.

The absorption properties of a medium could be clarified by investigating the extinction coefficient (*k*) upon exposing the medium by a certain wavelength. The extinction coefficient (*k*) is calculated from the following expression [40]:

$$k = \frac{\lambda\alpha}{4\pi} \quad (5)$$

where (λ) is the light wavelength and (α) absorption coefficient.

Figure 5a shows the wavelength dependence of extinction coefficient (*k*); for all MnS@ZnS heterostructures, the curves exhibited strong damping of the amplitude of the incident electric field at wavelengths above 300 nm. As the amount of ZnS increased in the nanocomposites, a blue shift trend was observed via displacing the *k*'s fall-point toward lower wavelengths as compared with MnS. In addition, the increase in *k*-value in the UV-range can be ascribed to the fundamental absorption peak of MnS [41].

Moreover, the refractive index of the different samples can be evaluated from the reflectance (*R*) using the following equation:

$$n = \frac{(R + 1) \pm \sqrt{3R^2 + 10R - 3}}{2(R - 1)} \quad (6)$$

As revealed in Fig. 5b, the refractive index decreased exponentially upon increasing the wavelength indicating the normal dispersion behavior of the samples. MnS exhibited a refractive index 2.3–2.2 in the wavelength range 200–300 nm and it decreased to 1.52 at higher wavelengths similar to what is obtained for annealed and non-annealed MnS films [33]; it exhibited high refractive index of 5.7 for annealed and 5.3 for non-annealed in the wavelength range 300–400 nm and then decreased to 1.5 for the range

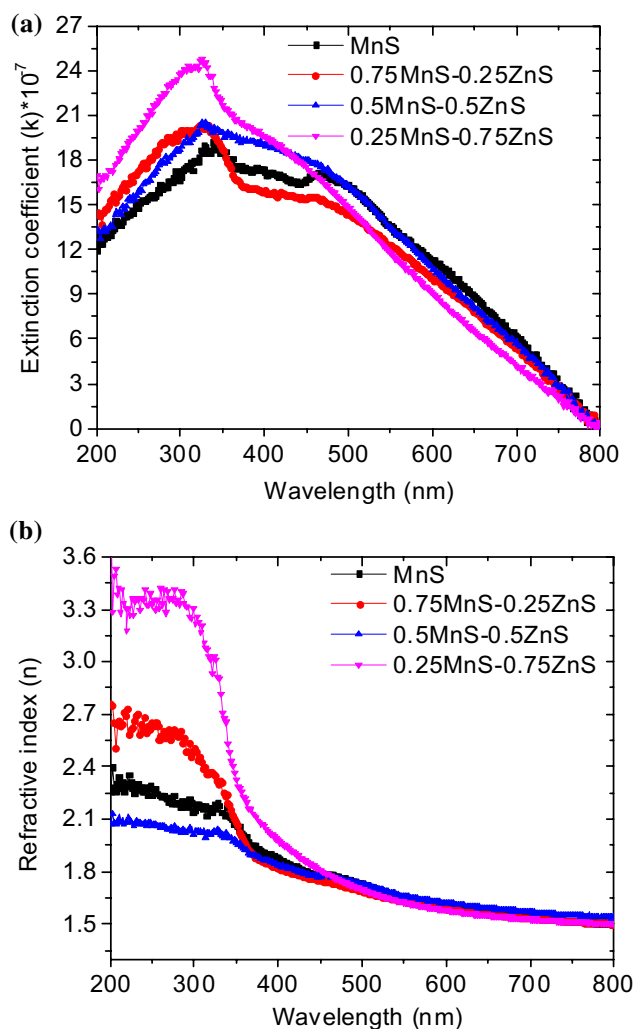


Fig. 5 Wavelength dependence of **a** extinction coefficient and **b** refractive index for MnS@ZnS nanocomposites system

400–1000 nm [33]. The low refractive index for the present MnS@ZnS nanocomposites is correlated with the small crystallite size, see X-ray section. The high refractive index indicated higher crystallinity and density of the sample compared with the sample with low refractive index [41]. For γ -MnS thin films annealed at 100–300, 400 and 500 °C, the refractive indices are increased 2–2.04, 2.09–2.90 and 2.14–3.38, respectively, in the visible region [42]. Upon alloying MnS with 25 and 75% ZnS, the refractive index is enhanced, but reduced as it is alloyed with 50% ZnS, reached its maximum value in 0.25MnS-0.75ZnS sample and minimum value in 0.5MnS-0.5ZnS sample. Materials with a low refractive index might be utilized as antireflection coatings in many applications [33].

The real (ϵ_r) and imaginary (ϵ_i) parts of the dielectric constant revealed the interactions between electrons and photons in the crystal. The two parts of the dielectrics for all samples

and also the dissipation factor ($\tan\delta$) were estimated using the following formulas [40]:

$$\varepsilon_r = n^2 - k^2 \quad (7)$$

$$\varepsilon_i = 2nk \quad (8)$$

$$\tan\delta = \frac{\varepsilon_i}{\varepsilon_r} \quad (9)$$

Figure 6 shows the real part of the dielectric constant and dielectric loss as a function of the wavelength for all samples; as the wavelength increased both the dielectric constant and dielectric loss reduced. Furthermore, the dielectric constant reached its maximum value for 0.25MnS–0.75ZnS nanocomposite and exhibited the minimum value in 0.5MnS–0.5ZnS nanocomposite sample as compared with nano-MnS sample. The increase in real constant indicated an enhancement in the optical response of the material [32].

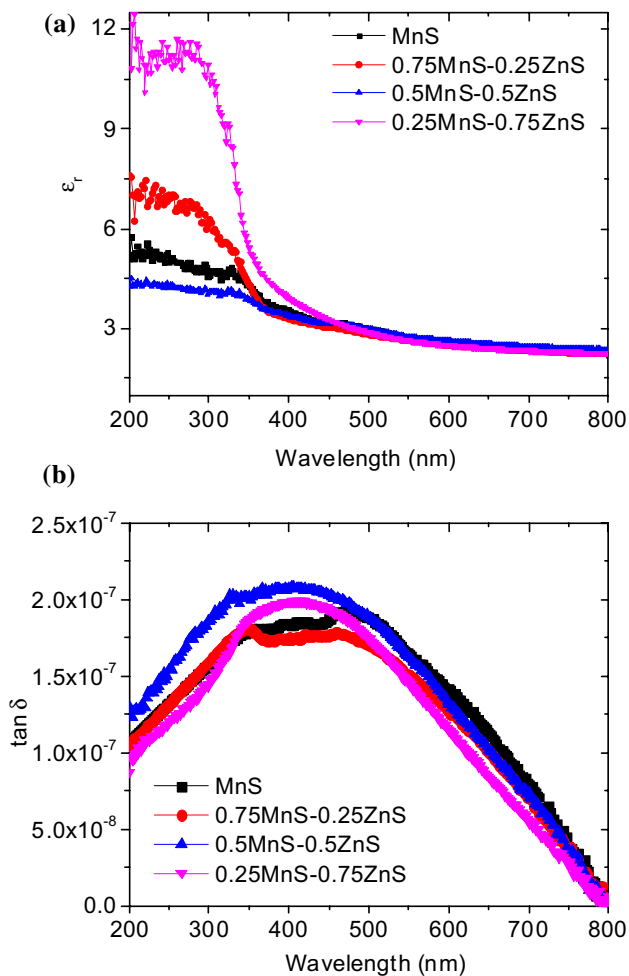


Fig. 6 Wavelength dependence of: **a** real dielectric constant, and **b** dielectric loss for MnS@ZnS nanocomposites system

Finally the optical (σ_{opt}) and the electric (σ_{ele}) conductivities are evaluated [40]:

$$\sigma_{opt} = \frac{\alpha n C}{4\pi} \quad (10)$$

where C is the light velocity.

Figure 7 depicts the σ_{opt} as a function of the photon energy, where it increased as energy increased. The optical conductivity is affected by both the refractive index and the absorption coefficient. Noteworthy, 0.25MnS–0.75ZnS revealed the highest value of σ_{opt} between all samples at high energy. This could be related to an increase in the density of

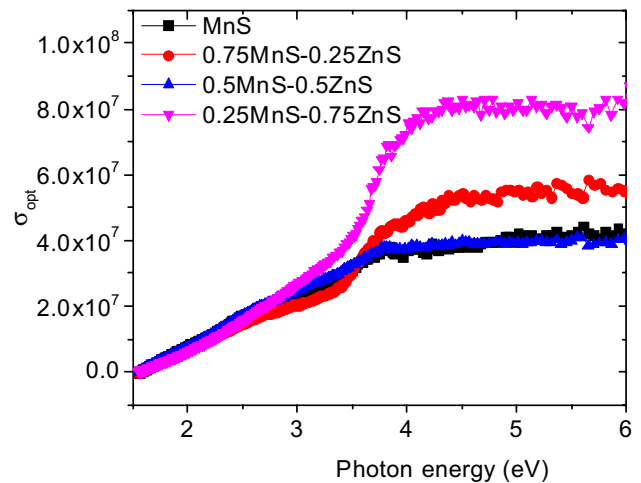


Fig. 7 Energy dependence of optical conductivity for MnS@ZnS nanocomposites system

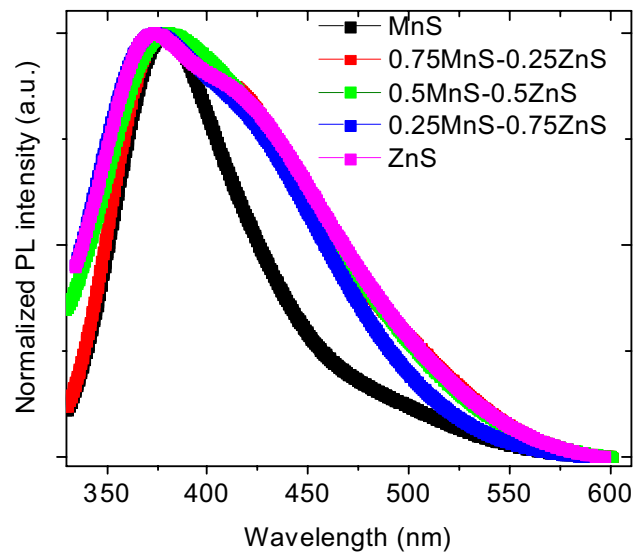


Fig. 8 Normalized photoluminescence spectra of MnS@ZnS hetero-structures samples

free charge carriers that undergo interband transition from the valence band to conduction band [40].

3.4 Photoluminescence analysis

Figure 8 shows the normalized photoluminescence (PL) intensities of MnS@ZnS heterostructures with different ratios between MnS and ZnS nanosamples at room temperature under 325 nm. The normalized PL emission spectra of ZnS and all nanocomposite samples are

broader than MnS sample which could be attributed to inhomogeneity of particle size distribution (the crystallite size of ZnS is around 4 nm, while crystallite size of MnS sample is around 20 nm, Table 1) and/or the existence of some surface state defects in these samples as compared with than MnS sample. Similar behavior was observed in the PL emission peak of ZnS/MnS/ZnS nanocomposites prepared by co-precipitation method which exhibited multiple asymmetrical and broadened peaks demonstrating the association of diverse luminescence centers in

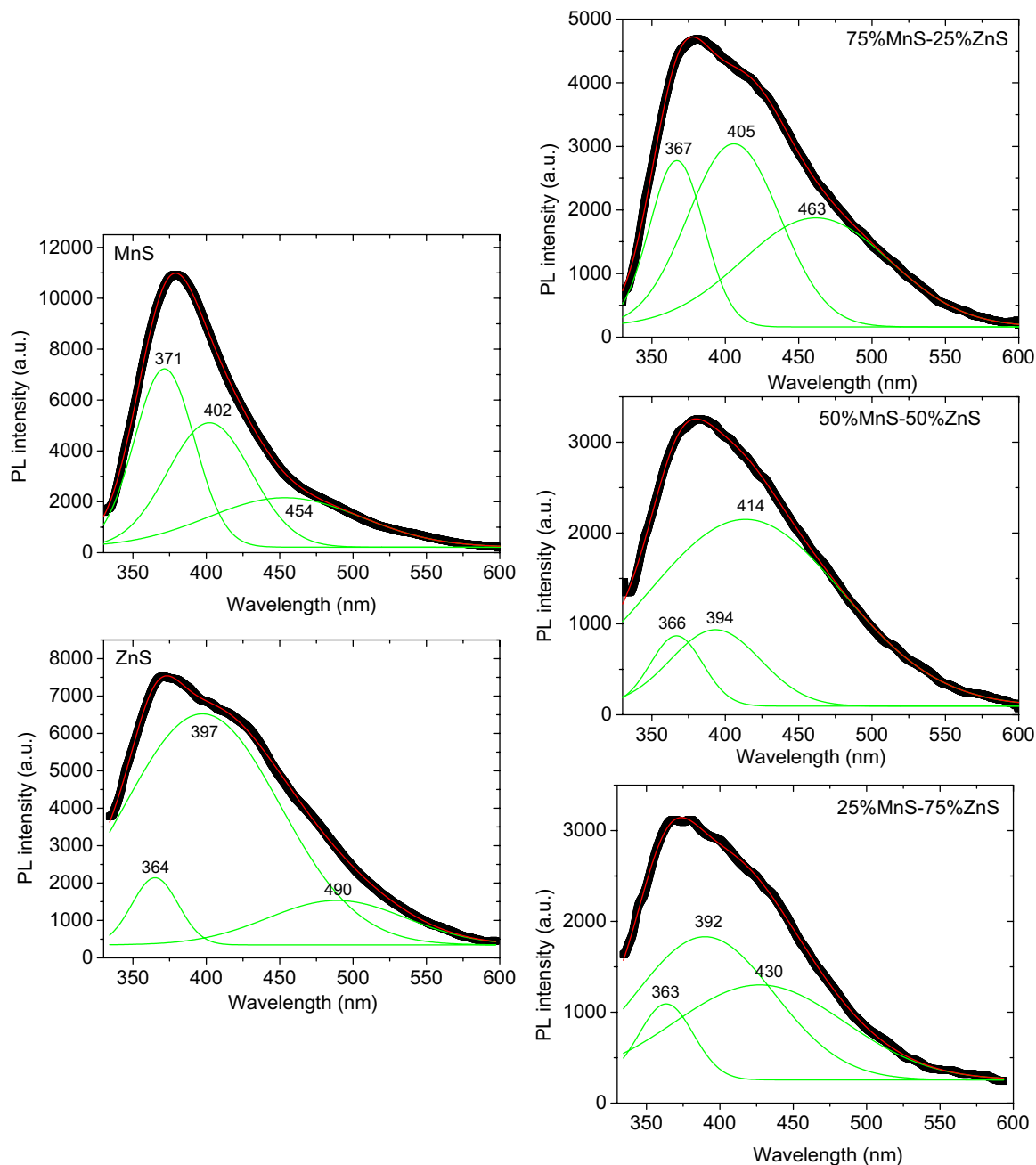


Fig. 9 Gaussian fitting for photoluminescence spectra of MnS@ZnS nanocomposite samples

the radiative processes [43]. Moreover, the composite samples are blue shifted as compared with MnS sample. This blue shift can be attributed to the difference between the values of energy bandgaps of MnS and ZnS phases. Worth notable, the PL intensities of intermediate MnS@ZnS nanocomposites are less than both MnS and ZnS samples, Fig. 9, which may be related to the changing of the crystallite size of the samples, Table 1. Figure 9 demonstrates the decomposition of PL emission spectra of all samples into sub-emissions using Gaussian function; all samples have three sub-emissions in (ultraviolet (UV), violet (V), blue (B) and green (G)) regions depending on the sample composition. MnS, ZnS, 0.75MnS–0.25ZnS, 0.5MnS–0.5ZnS and 0.25MnS–0.75ZnS samples exhibited PL sub-emissions at (371UV, 402V, 454B), (364UV, 397V, 490B-G), (367UV, 405V, 463B), (366UV, 394V, 414V) and (363UV, 392V, 430B) nm, respectively. Viswanath et al. [43] reported that the ZnS, prepared by chemical co-precipitation method in ambient atmosphere, emitted strong blue colors at 409, 432 and 463 nm [44, 45]. Also, ZnS synthesized by thermolysis technique exhibited violet, (blue, green), (blue, green), respectively [46]. Moreover, the annealed nano-ZnS emitted three PL colors in UV, blue and green regions [46].

According to many reports for ZnS, the interstitial sulfur energy levels are closer to the valence band than the interstitial zinc energy levels to the conduction band; meanwhile, sulfur vacancy states are nearer to conduction band edge than zinc vacancies states to the valence band edge [44, 45]. Accordingly, for present MnS@ZnS, the sub-emissions obtained around 405, 430, and 460 nm referred to interstitial sulfur, zinc interstitial and sulfur vacancies, respectively. Furthermore, hexagonal MnS nanoparticles, prepared by a microwave-assisted solvothermal process [47], emitted violet and green colors at 424, 468 and 531 nm, which associated with near band emissions (NBE); transitions between the conduction and valence bands representing bandgap energy. Tiwari et al. found that multiphase ($\gamma + \alpha$ at 200 °C and α above 300 °C) MnS thin film sputtered on glass substrates at different temperatures, exhibited two emissions at around 415 and 438 nm associated with band edge and trap state emissions [41]. They associated the first one to the transition of an electron from the MnS interstitial energy level to the valence band, while the second one was related to the defects and dislocations. So, for present MnS@ZnS, the emissions around 400–415 may refer to transition from MnS interstitial energy level to the valence band. Moreover, the sub-emission at 490 nm may result from Mn²⁺ 3d-configuration; similar to results obtained for nano-MnS synthesized using mild synthetic methods [48, 49]. The absence of red color in our measurements may be due to the existence of MnS₂ and MnS together with different structures in our samples, Table 1.

4 Conclusion

For the present MnS@ZnS heterostructures, zinc sulfide exhibited one phase ZnS (*F* 4 3*m*), while manganese sulfide sample manifested three phases: two cubics MnS *Fm* 3 *m* and MnS₂ *Pa* 3, and one hexagonal MnS *P* 6/3 *m* c. The intermediate samples of (1–*x*)MnS–*x*ZnS (*x*=0.25, 0.5 and 0.75) have different combinations from ZnS and MnS phases with different percentages. The cell parameter of cubic ZnS phase increased with the alloying parameter (*x*) indicating a tensile strain. HRTEM revealed a narrow size distribution and high agglomeration of the nanoparticles. SAED pattern demonstrated the existence of MnS and ZnS phases with different particle sizes in the composite samples. The 0.5MnS–0.5ZnS sample has the highest reflectance in the wavelength of less than 300 nm, while nanocomposites with *x*=0.25 and 0.75 have the highest reflectance for the wavelength above 500 nm. The direct bandgap energy determined for the samples *x*=0.0, 0.25, 0.5, 0.75 and 1.0 are 2.93, 2.76, 2.43, 2.39 and 3.2, respectively, indicating the gap energies for intermediate composites are less than for parent materials. The refractive index and dielectric constant have a maximum value in the case of 0.25MnS–0.75ZnS and a minimum value for 0.5MnS–0.5ZnS sample. 0.25MnS–0.75ZnS revealed the highest optical conductivity at high energy. The samples have three sub-emissions in ultraviolet, violet, blue and green regions depending on sample composition, phases included and type of defects in the samples.

Acknowledgements The authors are grateful to the Deanship of Scientific Research, King Saud University for funding through Vice Deanship of Scientific Research Chairs.

References

1. C.D. Pu, H.Y. Qin, Y. Gao, J.H. Zhou, P. Wang, X.G. Peng, J. Am. Chem. Soc. **139**, 3302 (2017)
2. T. Liu, Y. Li, J. Yin, J. Li, H. Wu, Physica E **116**, 113711 (2020)
3. Y.G. Chen, S. Zhao, X. Wang, Q. Peng, R. Lin, Y. Wang, R.A. Shen, X. Cao, L.B. Zhang, G. Zhou, J. Li, A.D. Xia, Y.D. Li, J. Am. Chem. Soc. **138**, 4286 (2016)
4. N.Y. Jamil, D. Shaw, Semicond. Sci. Technol. **10**, 952 (1995)
5. Z.K. Heiba, M.B. Mohamed, N.Y. Mostafa, Appl. Phys. A **125**(2), 132 (2019)
6. J. Kennedy, P.P. Murmu, P.S. Gupta, D.A. Carder, S.V. Chong, J. Leveneur, S. Rubanov, Mater. Sci. Semicond. Process. **26**, 561 (2014)
7. X.S. Fang, Y. Bando, M.Y. Liao, U.K. Gautam, C.Y. Zhi, B. Dierre, B.D. Liu, T.Y. Zhai, T. Sekiguchi, Y. Koide, D. Golberg, Adv. Mater. **21**, 2034 (2009)
8. V. Wood, J.E. Halpert, M.J. Panzer, M.G. Bawendi, B. Vladimir, Nano Lett. **9**, 2367 (2009)
9. J. Cai, S. Wang, K. Zhu, Y. Wu, L. Zhou, Y. Zhang, Q. Wu, X. Wang, Z. Hu, RSC Adv. **8**, 374 (2018)

10. R.S. Zeng, M. Rutherford, R.G. Xie, B.S. Zou, X.G. Peng, *Chem. Mater.* **22**, 2107 (2010)
11. D.G. Chen, R.J. Viswanatha, G.L. Ong, R.G. Xie, M. Balasubramanian, X.G. Peng, *J. Am. Chem. Soc.* **131**, 9333 (2009)
12. J. Zheng, W. Ji, X. Wang, M. Ikezawa, P. Jing, X. Liu, H. Li, J. Zhao, Y. Masumoto, *J. Phys. Chem.* **C114**, 15331 (2010)
13. Y. Zhao, J. Meng, X. Sheng, Y. Tian, *Adv. Optical Mater.* **4**, 1115 (2016)
14. J. Yuvaloshini, R. Shanmugavadivu, G. Ravi, *Optik* **125**, 1775 (2014)
15. Z.K. Heiba, M.B. Mohamed, M. Abdellatif, A.A. Albassam, *Appl. Phys.* **126**(7), 518 (2020)
16. Z.K. Heiba, A.A. Albassam, M.B. Mohamed, *Appl. Phys. A* **126**, 479 (2020)
17. M.B. Mohamed, Z.K. Heiba, N.G. Imam, *J. Mol. Struct.* **1163**, 442 (2018)
18. Z.K. Heiba, M.B. Mohamed, M.H.A. Kader, *J. Electron. Mater.* **47**(5), 2945 (2018)
19. Z.K. Heiba, M.B. Mohamed, N.G. Imam, *J. Mol. Struct.* **1136**, 321 (2017)
20. N.G. Imam, M.B. Mohamed, *J. Mol. Struct.* **1105**, 80 (2016)
21. Z.K. Heiba, M.B. Mohamed, N.G. Imam, *Ceram. Int.* **41**(10), 12930 (2015)
22. Z.K. Heiba, M.B. Mohamed, N.G. Imam, *J. Mol. Struct.* **1094**, 91 (2015)
23. Z.K. Heiba, N.G. Imam, M.B. Mohamed, *Mater. Sci. Semicond. Process.* **34**, 39 (2015)
24. Z.K. Heiba, M.B. Mohamed, N.G. Imam, *J. Alloy. Compd.* **618**, 280 (2015)
25. J. Rodríguez-Carvajal, *Phys. B (Amsterdam, Neth.)* **192**, 55 (1993)
26. L. Lutterotti, *Nucl. Inst. Methods, Phys. Res. B.* **268**, 334 (2010)
27. M. Elango, K. Gopalakrishnan, S. Vairam, M. Thamilselvan, *J. Alloys Compd.* **538**, 48 (2012)
28. J.X. Yang, S.M. Wang, X. Zhao, Y.P. Tian, S.Y. Zhang, B.K. Jin, X.P. Hao, X.Y. Xu, X.T. Tao, M.H. Jiang, *J. Crystal Growth* **310**, 4358 (2008)
29. B.S. Rema Devi, R. Raveendran, A.V. Vaidyan, *Pramana-J. Phys.* **68**, 679 (2007)
30. M. Kuppayee, G.K.V. Nachiyar, V. Ramasamy, *Mater. Sci. Semicond. Process.* **15**, 136 (2012)
31. S.B. Qadri, E.F. Skelton, D. Hsu, A.D. Dinsmore, J. Yang, H.F. Gray, *Phys. Rev. B* **44**, 153 (1999)
32. M. Girish, T. Dhandayuthapani, R. Sivakumar, C. Sanjeeviraja, *J. Mater. Sci.* **26**, 3670 (2015)
33. J. Yuvaloshinia, R. Shanmugavadivu, G. Ravi, *Optik* **125**, 1775 (2014)
34. J. Tauc, R. Grigorovici, A. Vancu, *Phys. Status Solidi* **15**, 627 (1966)
35. J. Akhtar, M. Afzaal, M. Banski, A. Podhorodecki, M. Syperek, J. Misiewicz, U. Bangert, S.J.O. Hardman, D.M. Graham, W.R. Flavell, D.J. Binks, S. Gardonio, P. O'Brien, *J. Am. Chem. Soc.* **133**, 5602 (2011)
36. F.J. Xu, B. Xue, F.D. Wang, A.G. Dong, *Chem. Mater.* **27**, 1140 (2015)
37. L. Luo, Y. Wang, S. Huo, P. Lv, J. Fang, Y. Yang, B. Fei, *Int. J. Hydrogen Energ.* **44**, 30965 (2019)
38. Z.Z. Ai, G. Zhao, Y.Y. Zhong, Y.L. Shao, B.B. Huang, Y.Z. Wu, X.P. Hao, *Appl. Catal. B* **221**, 179 (2018)
39. R.J.V. Michael, J. Theerthagiri, J. Madhavan, M.J. Umopathy, P.T. Manoharan, *RSC Adv.* **5**, 30175 (2015)
40. P.M. Dinakaran, S. Kalainathan, *Optik* **124**, 5111 (2013)
41. P. Tiwari, J. Jaiswal, R. Chandra, *J. Appl. Phys.* **126**, 213108 (2019)
42. C. Ulutasa, M. Gunes, C. Gumus, *Optik* **164**, 78 (2018)
43. R. Viswanath, H.S. Bhojya Naik, G.S. Yashavanth Kumar, P.N. Prashanth Kumar, K.N. Harish, M.C. Prabhakara, *Spectrochimica Acta Part A* **125**, 222 (2014)
44. R.N. Bhargava, *J. Lumin.* **70**, 85 (1996)
45. N. Karar, F. Singh, B.R. Mehta, *J. Appl. Phys.* **95**, 656 (2004)
46. M.B. Mohamed, *Int. J. Appl. Ceram. Technol.* **17**(2), 823 (2020)
47. M.M. Hosseini-Hajivara, F. Jamali-Sheinib, R. Yousefic, *Solid State Sci.* **93**, 31 (2019)
48. T. Veeramanikandasamy, K. Rajendran, K. Sambath, *J. Mater. Sci.* **25**(8), 3383 (2014)
49. N. Moloto, M.J. Moloto, M. Kalenga, S. Govindraj, M. Airo, *Opt. Mater.* **36**, 31 (2014)

Publisher's Note Springer Nature remains neutral with regard to jurisdictional claims in published maps and institutional affiliations.